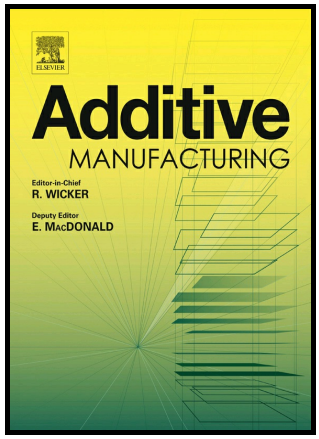

Critical assessment of the impact of process parameters on vertical roughness and hardness of thin walls of AlSi10Mg processed by laser powder bed fusion

O. Poncelet, M. Marteleur, C. van der Rest, O. Rigo, J. Adrien, S. Dancette, P.J. Jacques, A. Simar

PII: S2214-8604(20)31173-8

DOI: https://doi.org/10.1016/j.addma.2020.101801

Reference: ADDMA101801

To appear in: *Additive Manufacturing*

Received date: 6 July 2020
Revised date: 4 December 2020
Accepted date: 17 December 2020

Please cite this article as: O. Poncelet, M. Marteleur, C. van der Rest, O. Rigo, J. Adrien, S. Dancette, P.J. Jacques and A. Simar, Critical assessment of the impact of process parameters on vertical roughness and hardness of thin walls of AlSi10Mg processed by laser powder bed fusion, *Additive Manufacturing,* (2020) doi:https://doi.org/10.1016/j.addma.2020.101801

Critical assessment of the impact of process parameters on vertical roughness and hardness of thin walls of AlSi10Mg processed by laser powder bed fusion.

O. Poncelet[1], M. Marteleur[1], C. van der Rest[1], O. Rigo[2], J. Adrien[3], S. Dancette[3], P. J. Jacques[1], A. Simar[1]

[1]UCLouvain, Institute of Mechanics, Materials, and Civil Engineering (IMMC), IMAP, Place Sainte Barbe, 2, 1348 Louvain-la-Neuve, Belgium.
[2]Sirris, T-ADD Team, 4102 Seraing, Belgium.
[3] University of Lyon, INSA Lyon, CNRS UMR5510, Laboratoire MATEIS, F-69266 Villeurbanne, France.

E-mail: olivier.poncelet@uclouvain.be

Abstract. This work deals with the impact of prominent process parameters in laser powder bed fusion (L-PBF) technique, also called selective laser melting (SLM), on relevant properties of AlSi10Mg such as surface roughness and hardness. More particularly, the influence of scanning strategies, track energy density (TED), and of the offset between the contours and the bulk hatching were scrutinized. Basic thin structures such as single wall tracks (SWT) and ultra thin walls (UTW) were used to isolate the effect of the TED and of the offset between parallel melt pool tracks on the vertical roughness, respectively. It is shown that the TED reduces the level of roughness mostly due to a geometrical effect. The optimum range of TED is shown to be at the beginning of the keyhole conditions, at the expense of the amount of sub-surface porosities and of hardness. Increasing the offset also allows reducing the roughness. Thicker structures with contours and bulk hatching were also used and brought the same conclusions. In this work, low levels of roughness (about 4 µm)) have been obtained on vertical walls without any post-treatment but at the expense of the mechanical properties.

Keywords: L-PBF, SLM, AlSi10Mg, roughness, hardness, process parameters, contours, bulk hatching, sub-surface porosities.

Nomenclature: TW: thin walls; SWT: single wall tracks; UTW: utra thin walls; CF: contour first; BF: bulk first.

1. Introduction

Laser powder bed fusion (L-PBF, ASTM Standard F2792 (1)), is more and more used for the processing of metallic components. Owing to their good strength/weight ratio combined with a high thermal conductivity, aluminum alloys, including AlSi10Mg alloy, are well adapted materials for applications such as heat exchangers processed by L-PBF. However, defects associated to this specific combination of materials and process, such as high surface roughness and presence of porosities still limit the applications where mechanical performances are restrictive. Indeed, surface roughness

of parts made of AlSi10Mg alloy by L-PBF is of large concern in aerospace and automotive industries since it directly impacts the fatigue life (2; 3; 4; 5) and corrosion properties (6; 7; 8). Despite this large importance of surface roughness, hardly any studies investigated in details its origin and its evolution with process parameters. Furthermore, published studies investigated the influence of process parameters on the top surface roughness (upskin) (9; 10; 11; 12; 13; 14; 15; 16) while side (vertical) roughness has been studied to a lesser extent (17; 18; 15; 16). While inclined surfaces lead to a large roughness due to a stair stepping effect related to the intrinsic stratification process (19; 20; 21), roughness on vertical surfaces is not yet fully scrutinized. If it is clear that defects such as spatters, satellites or balling increase the vertical roughness (17; 18), the relationship between process parameters, scanning strategies and roughness is not yet clearly established, even though there impact has been observed (22; 23; 15; 16). Moreover, while previous studies showed that increasing the volumetric energy density (VED) seems to reduce the side roughness (17; 12; 18) below a R_a of 5 µm, the impact of this increase of energy on porosity or on the mechanical properties is not yet studied. In order to investigate the factors influencing the vertical roughness, thin-wall samples and other structures were processed using a wide range of parameters. The level of sub-surface porosity as well as the hardness were simultaneously investigated. This work provides a systematic study to assess the origin of vertical roughness of L-PBF products and gives guideline to obtain a desirable net-shaped structure.

In L-PBF, any processed object is built by a succession of parallel and stacked unit cells, called laser tracks, melt pool tracks or single tracks. It is well established now that a part is also divided into two different areas during the slicing (the stratification process): the bulk hatching (core or in-fill plane) and the contours (the hull, borders or outer shell) which are the object boundaries (24). Both areas are processed following different parameters (mainly, laser power and scanning speed). Parameters for the bulk hatching are logically selected to obtain a porosity-free material while parameters for the contours are chosen following surface roughness considerations. In the case of L-PBF, roughness can thus be considered as a topographical measurement of the melt pools constituting the contours. It is also well established now that the level of bulk porosities is directly linked to the bulk melt pool track stability (25; 26; 27) and thus related to the process parameters (28; 29; 30; 31). A process window in which the melt pool tracks are stable can then be established. However, no such conclusion has been drawn yet for the contour process parameters.

The first part of this work describes a methodology systematically assessing the processing parameters to reach a low level of vertical roughness. The most basic structure, i.e. a stack of single tracks, called single wall track (SWT) in this work, is used as test sample. This structure, mostly used to investigate the L-PBF process behavior (32; 33), allows highlighting the impact on the roughness of two important process parameters, i.e. the laser power and the scanning speed. Those parameters can then be analyzed independently of the building strategies (contours, bulk, ...). Hardness of SWT was also measured to investigate the evolution of the mechanical properties with the laser power and the scanning speed, as the microstructure of such alloy quickly evolves with heat and thus with the process parameters (34). L-PBF AlSi10Mg has a hierarchical microstructure where large grains present a fine cellular-dendritic solidification structure with submicron-sized primary Al-cells and an intercellular Si network.

Moreover, this heterogenous microstructure follows the shape of the melt-pools and is divided in 3 distinct microstructures: the fine zone, the coarse zone and the heat affected zone (29; 35). This microstructure directly affects the hardness properties of the alloy and is very sensitive to its thermal environment and to thermal treatments (36). Indeed, within the melt-pools themselves, hardness gradient have been observed (from 150 HV in the fine zone to 110 HV in the coarse zone) due to different cooling rates within the pool (37; 38). Depending on the process parameters and the building temperature, hardness of as-built L-PBF AlSi10Mg can range from 90 HV (39) to 125 HV (40; 41; 36; 42) or above 130 HV (43; 34).

While only laser power and speed are investigated in the case of SWT, contiguity of melt pool tracks, e.g. in the case of contours and bulk hatching, can cause a change of the solidification morphology (44) (due to wetting conditions between tracks), impacting directly the roughness. Accurate modeling of the L-PBF process predicts that gravity, surface tension and subsequent wetting or capillarity forces are responsible for melt pool stabilities and morphology (45; 46; 47; 48; 49; 50). The second part of this work deals with the interaction of adjacent melt-pools by using a structure called ultra thin-walls (UTW), composed of two parallel SWT.

Finally, the third part of this work investigates thicker structures. 600 µm-thick structures (thin-walls, TW) with a bulk hatching area were processed to confirm the predictions made from the analysis of the SWT and UTW structures. New process parameters have to be considered as a result of the bulk hatching area, the scanning strategy and the offset. Indeed, there are two options to process the structures; either the bulk hatching is processed before the contours (bulk first strategy (BF)) or the contours are processed first (contours first strategy (CF)). Up to now, reported studies on roughness have been mostly performed with a BF strategy (13; 18; 51; 52) while the CF strategy has been less studied (9). In this work, 600 µm-thick structures were selected because they are representative of the wall thickness in applications such as heat exchangers, in which the level of roughness is important to keep control of the heat transfer, pressure drop and eventually fatigue resistance.

As a conclusion, the optimized set of parameters was tested on thin-walls and on bulk cubic structures with a first insight in the mechanical behavior owing to hardness measurements.

2. Materials and Experimental Procedure

*2.1. **Manufacturing by L-PBF***

L-PBF samples of AlSi10Mg alloy were processed with a ProX® DMP 200 (3D Systems Inc.) machine with a laser operating at 1075 nm wavelength, a spot size of 70 µm and 273.6 W maximum power. AlSi10Mg gas atomized spherical powder with an average diameter of 15-53 µm was provided by TLS Technik. The layer thickness was fixed at 30 µm for all samples. The build-plate was not heated during the L-PBF process and is initially at room temperature. The manufacturing was performed in an argon gas atmosphere, with a residual level of O_2 concentration smaller than 500 ppm. Samples were processed without support parts, directly on the build-plate. No

post-treatments were applied.

The process window has been identified prior to the present work by studying the stability of single tracks as proposed in previous works (26; 53). Track energy density (TED) or linear energy density (LED, defined as the power divided by the scanning speed) between 120 J/m and 200 J/m have been established as the boundaries of process window, in good agreement with previous work (26) for AlSi10Mg alloy. A TED level of 194 J/m (232.5 W at 1200 mm/s) for the bulk hatching was selected in this work as the standard parameters.

Figure 1 illustrates the three main geometries investigated in the present work. Single wall track samples (SWT), 10 mm in height and width, were processed by stacking single tracks (Figure 1.a). The impact of power and scanning speed on the arithmetic roughness (R_a) and on the hardness was considered. Roughness was measured on both SWT faces. As no R_a differences between the faces were noticed, results will be presented as a mean of both faces. It is worth noting that the laser starting point did not change from one layer to another.

A second set of specimens, called ultra-thin wall samples (UTW) consists in two parallel tracks or SWT (Figure 1.b), 10 mm in height and width. The impact of the hatch-space between the two tracks on the roughness was also considered at two different TED levels. The face constituted by the first contour is called "face 1" while the face constituted by the second contour is called "face 2". R_a was measured on each face. The laser starting point did not change between each layer for most samples. However, one sample was processed with a moving starting point, following the diagonal (y-z plane) of the sample (allowing to process the sample presented in Figure 15). Hardness measurement were not performed on those samples as the microstructure does not change with the chosen offsets.

Thin-wall samples (TW) are 600 µm-thick walls, 10 mm in height and width with a bulk hatching and contours (Figures 1.c and d). The bulk hatching and the contours were processed with their own set of parameters (laser power and scanning speed). Unless mentioned, bulk hatching was processed at 232.5 W (85 % of P_{max}) and at a scan speed of 1200 mm/s, a hatch space of 100 µm and a scanning rotation of 90 between each layer, as depicted on Figure 1.c and d. Bulk hatching and contours were processed following two distinct strategies. The laser starting point of the contours did not change from one layer to another. The laser starting point of the bulk changed between each layer, as indicates on Figure 1.c and d (between layer "n" and "n+1").

In the first strategy (Figure 1.c), contours are processed first (CF strategy). The second strategy is the opposite (Figure 1.d), i.e. the bulk hatching is firstly processed (BF strategy). When one strategy is selected, it is applied to each layer of the same sample. Within these two strategies, several parameters were varied for the contours: laser power, scanning speed and the offset. The offset is defined here as the distance between contours and the bulk hatching (Figures 1.c and 1.d). The contour is processed asymmetrically as the starting point is always on the same thin-wall face (depicted on Figure 1.d). The face constituted with the contour processed first is called "face 1" and the face constituted with the second contour is called "face 2". Roughness measurements were thus performed on each face individually.

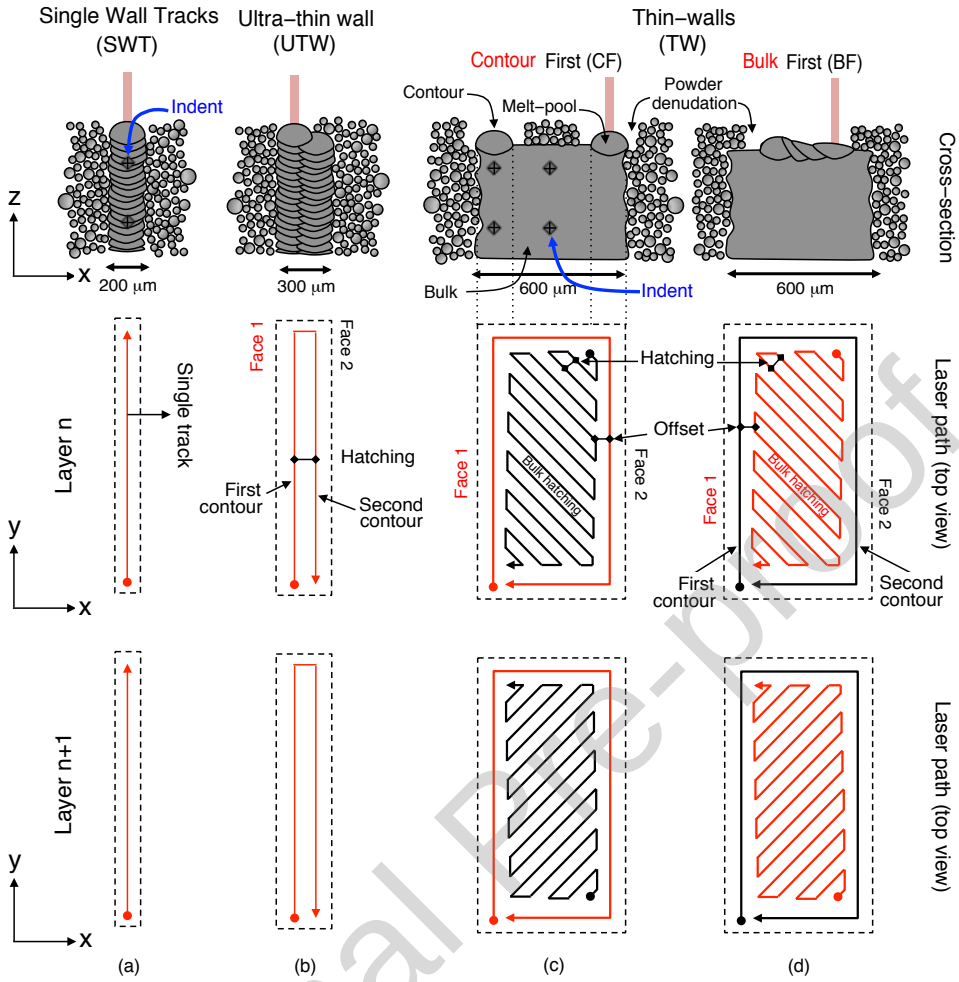

Figure 1. Schematic representation of the four main types of samples and their respective laser track patterns; (a) single wall track (SWT) samples, corresponding to a stack of single tracks; (b) ultra-thin wall (UTW) samples, corresponding to two parallel SWT; 600 µm-thick thin-wall (TW) samples with (c) contour first (CF) strategy and (d) bulk first (BF) strategy. The mentioned thicknesses will be slightly affected by the laser parameters. Location of hardness indents are shown on the x-z plane.

Finally, optimum parameters found with SWT, UTW and TW samples were tested on TW samples and on a 10 mm-side cube. The cube was processed with a CF strategy. The roughness and hardness of those samples were also measured. Hardness measurements were performed on the contours and on the bulk hatching in the xz-plane.

For the present study, 10 batches were processed. The number of samples per batch was kept similar (60 ± 10) to maintain the job load. Indeed, small roughness variations can be measured when the job load changes drastically. Each series of

the same parameter were done on the same job. A limited number of samples were produced on different batches to assess reproducibility. Thin walls with two different contour TED have been produced perpendicularly to each other, in order to check the impact of the orientation as it can affect the roughness (54). No difference was observed. This will thus not be further reported. The build-plate is an Al5Mg (wt% Mg) square of 141 mm by 141 mm and is 15 mm-thick. Samples were widespread on the plate and equally separated by a distance of 10 mm. The height of the samples was fixed to 10 mm. Taller samples (100 mm) were produced to check the impact of the height but no significant difference was found.

2.2. ***Characterization techniques***

Roughness analyses were carried out by white light interferometry, referenced as coherent scanning interferometry (CSI) (55) with a MSA-500 Micro System Analyzer (Polytec) built on a vibration-isolation table (SUSS, VIT80x range). CSI is a powerful method to perform topographical analyses. Measurements were carried out following the *Good Practice Guide No 116* (56) and some other works (57; 58; 59) in order to obtain reliable data. A x10-objective was used to insure a good trade-off between field of view (880 x 660 µm map) and adequate lateral resolution (635 nm x 635 nm) and gave a numerical aperture of 0.3. Raw measurements were analyzed with Polytec's TMS software 2.0 (Topography Measurement System). The measurements were carried out in short coherent mode. The cutoff wavelength was set to 800 μm for λc and 2.5 μm for λs for each profile analyzed in agreement with the EN ISO 13565-1 standard. 5 sampling length of 130 μm (limited here by the field of view) were used. Each measured topographical map was divided into 60 vertical profiles (z-direction) and a mean arithmetic average roughness (R_a) was computed out of these profiles. In this work, R_a was considered because it is one of the most adopted texture parameter (57) and it is thus largely used. Even though this parameter does not bring much information about the type of roughness, R_a is mainly used in many applications. On each sample, 8 maps were acquired (4 per face) for a total area of 3.85 mm^2, insuring a reliable value of the arithmetic roughness (60). Error bars are the standard deviation between the maps and show how the data are scattered. Indeed, the local nature of CSI measurements tends to increase the scattering of the data. R_z and R_{max} were also measured on each samples but gave the same trends as R_a (see supplementary material). Thus, only R_a will be presented here. It is worth noting that our measurements cannot directly be compared with S_a measurements as no surface filtering is used here.

Hardness was measured with a DuraScan G5 from EMCO-TEST with a Vickers tip indenting with 200 g (HV 0.2). The measurements were carried out on x-z cross-sections (Figure 1) of samples polished down to 1 µm. Ten indents were performed per measurement to insure reliable data. However, the heterogeneous microstructure of AlSi10Mg processed by L-PBF (29) may increase the scattering in hardness (38). As indent sizes were about 50 µm large, they were performed with a 300 µm-space between them in the building z-direction. Indents were performed in the middle of the SWT (Figure 1.a). For hardness measurements of TW, indents were performed in the middle of the contour and in the middle of the bulk (Figure 1.c).

The melt-pool structure of the samples was characterized after grinding and polishing steps, followed by a chemical etching using a Keller's etchant. Scanning

electron microscopy (SEM) images were performed only on some relevant samples. Several TW samples were also analyzed by X-ray computed micro-tomography (61; 62) in order to characterize the internal porosity. A 1 mm-thick section (in y-direction) was extracted from each sample for the measurements (giving parallelepipedic dimensions of 600 µm x 1 mm x 10 mm in xyz directions, respectively). The acquisitions were performed with a vtomex laboratory X-ray computed tomograph (GE Phoenix X-Ray GmbH) equipped with a 160 kV nano-focus tube, a tungsten transmitting target, and a 1920 x 1536 pixels Varian detector. Scanning parameters were set at 80 kV tube voltage and 280 µA current with a voxel size of 2 μm^3. A full analysis consists of 600 $2D$ radiographs and an averaging of 3 images at each step angle. The exposure time for one radiograph was set to 0.5 s. The volumes were then reconstructed by a filtered back projection Feldkamp-algorithm. The reconstructed data were finally processed and visualized with ImageJ/Fiji shareware (63). Data for each sample were binarized in order to visualize the porosities and to compute a mean density.

3. Results and Discussion

3.1. ***Single wall tracks: effect of laser power and scanning speed on roughness***

Figure 2 summarizes roughness and hardness measurements performed on single wall track (SWT) samples built at a fixed scanning speed of 200 mm/s (Figure 2.a) or at a fixed power of 273 W (Figure 2.b), for a large range of TED. Furthermore, several optical microscopy images illustrate how the microstructure changes with the level of TED. In both cases, the roughness does not change monotonously with the TED parameter. A minimum R_a can be reached, depending on the laser scanning speed and power. Topological maps show that surface defects are also different depending on the TED level.

A minimum roughness of 5.9 µm is reached for a TED level around 1000 J/m for a scanning speed of 200 mm/s (Figure 2.a). It is worth noting that this TED level corresponds to the transition between self-balling (characterized by a fluctuating melt pool depth) and keyholing mode in this case. At high energy density, balling appears due to the Plateau-Rayleigh instability (47; 49; 44; 53), caused by a surface energy minimization of the melt pool. On the other hand, keyhole instability is observed when the energy injected in the melt pool becomes too large (64). Material vaporization within the melt pool induced by an excessive amount of energy causes the melt pool to be unstable (65). In keyholing mode, large porosities appear in the center of the SWT, as shown on the micrographs in Figure 2.a. The increasing R_a in keyhole conditions (above a TED of 1000 J/m) is due to an increasing amount of sintered powder on the side of the SWT samples. Increasing the level of TED also increases the time spent by the samples at high temperature, thus enhancing the powder sintering. Large clusters of sintered powder then appear at very large TED level, as shown by the corresponding topographical maps in Figure 2.a. As clusters are not homogeneously distributed, this increases the roughness scattering. On the contrary, very few sintered powder is present in the optimum range (around a TED of 1000 J/m).

At fixed power, Figure 2.b shows that R_a evolves similarly with TED as observed for the previous case. The lowest R_a, 4.5 µm, is obtained near the keyhole conditions

as well, around 700 J/m in this case. There is still a roughness decrease at low TED for 273 W but large porosities appear due to the too low energy density for this structure. Similarly to Fig. 2.a, powder sintering is also observed for larger TED.

In both cases studied here, a coarsening of the microstructure within the melt-pools by increasing the level of TED is observed. Melt-pool microstructure of AlSi10Mg is divided in 3 distinct zones, called fine zone, coarse zone and heat affected zone (HAZ) (29). Fine zones are the core of the melt-pools where the size of the cells of the microstructure is the smallest. Coarse zones are the border of the melt-pools, where the size of the cells is larger than in the fine zone. The HAZ are just outside melt-pool boundaries where the microstructure is globularized. Figure 3 presents SEM micrographs of three SWT for which hardness and roughness are provided in Figure 2.a. The microstructure within the three zones are affected by the level of TED (Figure 3.a). The size of the cells within each zone increases by increasing the level of TED. The size of the cells doubled when the power was increased from 109 W to 274 W (Figure 3.b), explaining the hardness decrease. Indeed, strengthening in materials is induced by hindering the dislocation glides through solid solution hardening, precipitation strengthening or by reducing grain size. In the case of the as-built L-PBF AlSi10Mg, previous studies have shown that strengthening mechanism is governed by the size of the fine microstructure rather than by the grain size (29; 26; 66), where the Si network forming the cell boundaries pins dislocations and induces Orowan looping mechanism (67). Coarsened microstructure leads then to a decrease of the hardness (37; 38).

This microstructure coarsening, due to a longer time at high temperature (29; 68), induces a decrease of the hardness, from 127 HV to 108 HV at a fixed scanning speed (Figure 2.a) and from 132 to 108 HV at a fixed power level (Figure 2.b). Indeed, similar hardness decrease can be observed on AlSi10Mg parts after heat treatment (54; 69; 70). The heterogenous microstructure observed within the SWT (Figure 3.a) and the size of the indents ($\pm$ 50 µm) are responsible for the hardness data scattering. Indeed, hardness on the edges of the melt pools (coarse and HAZ zones) is lower than in the core of the pools (37; 38) (fine zone). Moreover, indents performed on the thinner samples are near the free-wall surface, which may also induce some scattering due to border effects on plasticity confinement.

However, the observed trends are in line with the microstructure evolution (i.e. the coarser the microstructure, the softer is the material).

Figure 2 thus shows that a minimum roughness is obtained for a level of TED close to the one bringing keyhole instability. A process window minimizing R_a thus exists, just as it is the case for maximizing the density. However, the required level of TED is significantly larger to minimize R_a than to maximize the density (120-200 J/m). As a consequence, conditions for contours and bulk hatching must be different. It is worth mentioning that other conditions of fixed scanning speed and power were also tested and led to the same conclusions (see supplementary material).

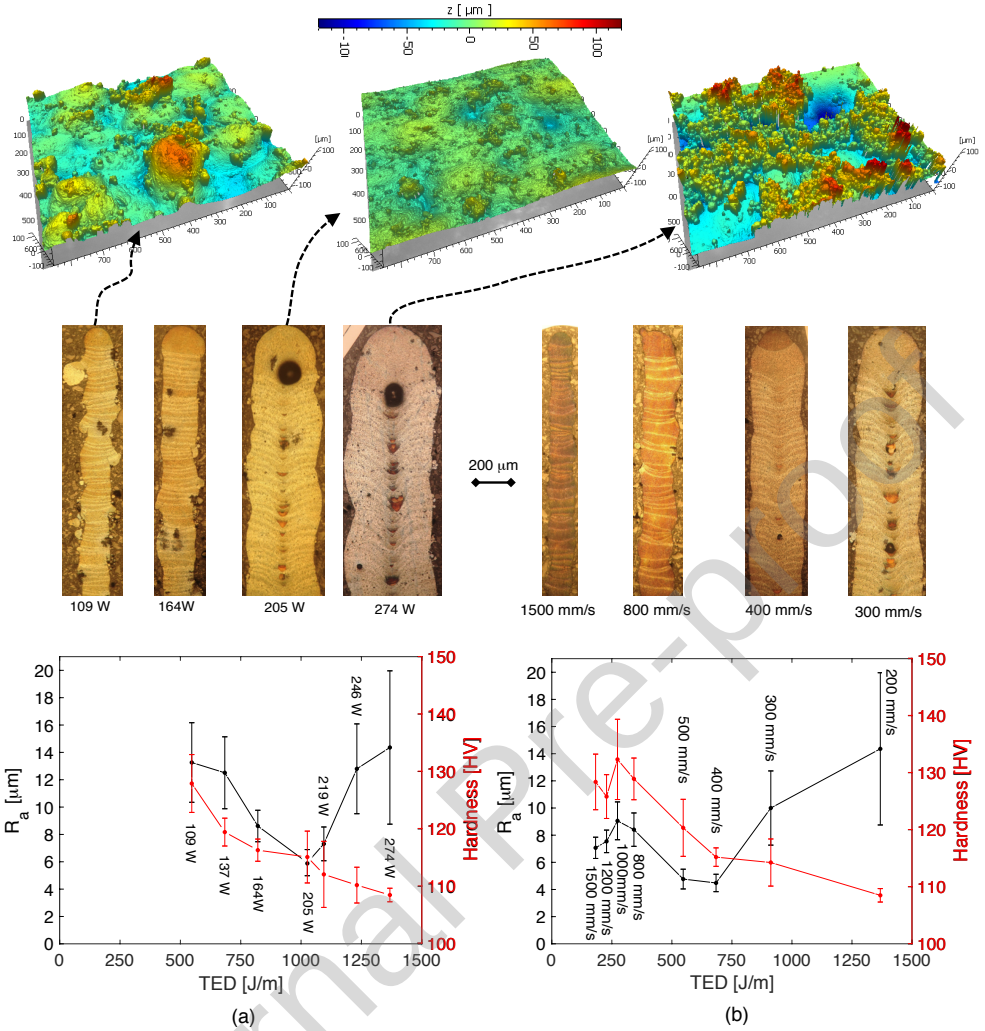

Figure 2. Evolution of roughness and hardness of SWT as a function of TED for (a) a fixed scanning speed of 200 mm/s and for (b) a fixed laser power of 273 W. Optical microscopy images of SWT cross-sections illustrate the internal structure of the SWT for specific TED levels while topographical maps corresponding to extreme processing conditions are also provided.

*3.2. **Ultra-thin walls: effect of the offset between tracks on roughness***

Using SWT samples thus allows finding a process window for contours leading to a minimum level of roughness. This simple structure discriminates in Section 3.1 the effect of the scanning speed and laser power from the offset since there is no bulk hatching in this case. The effect of an offset (or hatch space) between melt pool tracks on the roughness is now investigated by using structures called ultra thin walls (UTW, Figure 1.b).

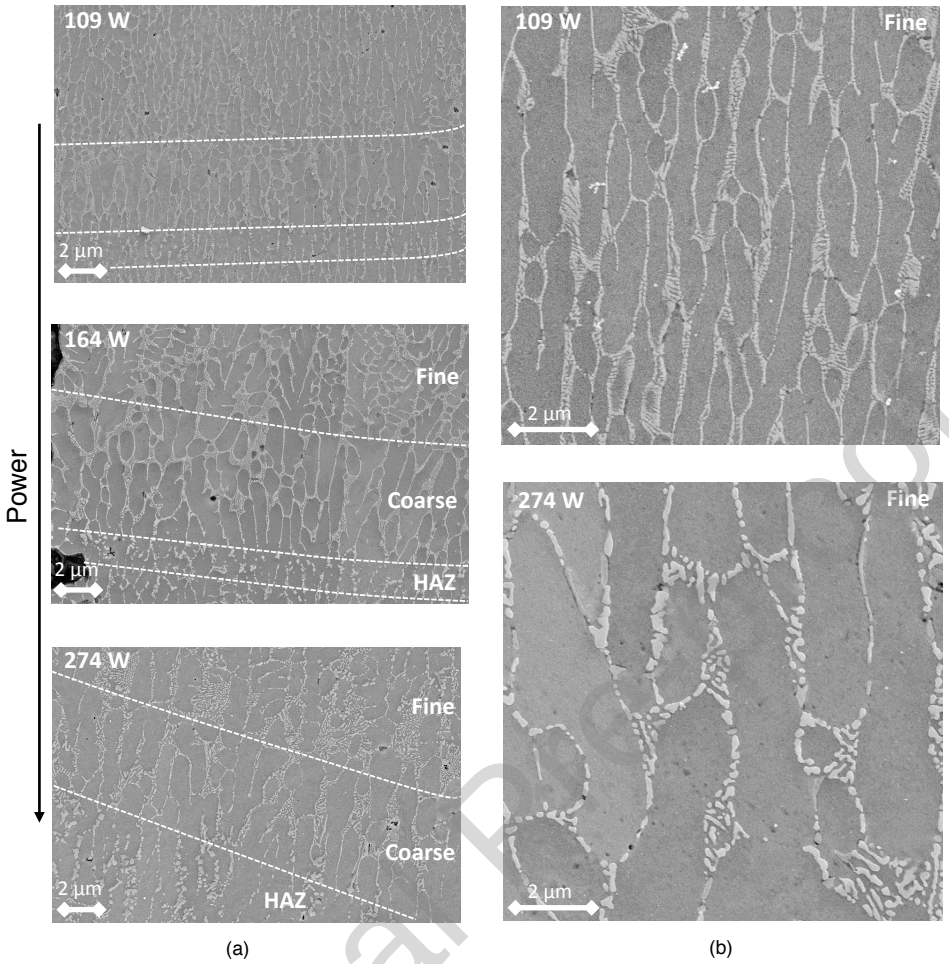

Figure 3. SEM micrographs of SWT processed at 200 mm/s with different power showing (a) the three different microstructure zones. (b) Zoom on the fine microstructure for the two extreme power. Micrographs were taken on the top of the SWTs. No inhomogeneities were found in the z-direction as SWT are simple structures and small in height.

Figure 4 presents roughness measurements performed on both sides of several UTW samples. R_a is presented as a function of the distance between two parallel tracks. A 100 µm hatch space was chosen as a starting point and was increased by steps of 30 µm. The samples were processed with two levels of TED. R_a of SWT with the corresponding TED level are also given as a reference.

R_a value of "face 1" (face corresponding to the first processed track) with a TED level of 194 J/m is not much impacted by the distance between the tracks. On the contrary, R_a value of "face 2" decreases gradually as the offset increases, converging towards the R_a value of SWT specimen. In the case of a higher TED level, the conclusions on roughness behavior are similar. The R_a value of "face 2" decreases with the offset.

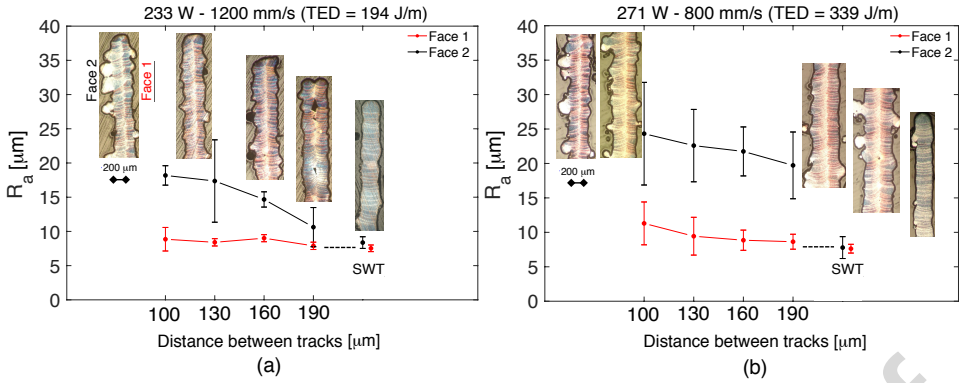

Figure 4. Evolution of the arithmetic roughness of first (in red) and second (in black) contour of UTW samples as a function of the distance between tracks, processed with a TED level of (a) 194 J/m and (b) 339 J/m. The corresponding power and scan speed are indicated on top of the graphs. Corresponding optical microscopy images of x-z cross-sections are also provided. R_a level of SWT specimens processed with the same level of TED are indicated as a reference.

Micrographs of Figure 4.a show that the two SWT constituting the UTW start to separate for a hatch space of 190 µm, leaving pores between them. In the case of the higher TED level, the two tracks are not yet separated for an offset of 190 µm due to a better overlapping of larger melt-pools.

The results of Figure 4 clearly show that the distance between parallel tracks influence the resulting roughness. Changes of the melt pool morphology between parallel tracks have already been reported on L-PBF of stainless steel (71). This effect is even more evidenced when TED increases as a result of the melt pool widening, thus increasing interactions between superimposed melt pool tracks. Optical microscopy images of Figure 4 show that this interaction induces the melt pool of "face 2" to flow outward, especially for the distance of 100 µm. Those protuberant melt pools have a huge impact on roughness. The distance between the contours and the bulk hatching, namely the offset, has thus a direct impact on roughness.

3.3. ***Thin walls: effect of the strategy and offset***

Figure 5 presents the evolution of the arithmetic roughness of thin-wall samples (TW) as a function of the offset, for both building strategies, i.e. 'bulk first' and 'contour first'. SEM micrographs of TW surfaces (y-z plane) for the two extreme offsets are also provided. Figure 5 highlights two first-order effects related to the building strategy and the amplitude of the offset. Increasing the offset has a significant impact on the BF strategy, decreasing R_a from 35 µm down to 13 µm. However, it is almost effectless in the case of CF strategy, for which the mean level of R_a is about 9 µm for all offsets. For the same offset, a CF strategy always leads to a lower R_a than for the BF strategy. Many other TED levels were also tested and showed similar trends (see supplementary material). SEM micrographs of Figure 5 also show that the large level of R_a in BF strategy is mainly due to huge protuberances (of about 150 µm).

The amount of protuberances decreases when increasing the offset. Sintered powder is also observed on the surface but does not impact significantly R_a since the size of the powder is much smaller than the protuberances. In the case of the CF strategy, SEM micrographs show no more protuberances. Not much sintered powder can still be observed.

It is worth noting that the level of R_a of "face 1" (corresponding to the first processed contour) is quasi systematically slightly lower than the R_a level of "face 2" in the case of the BF strategy, for each offset. This difference is less or even not noticeable anymore in the case of the CF strategy, whatever the value of the offset. However, the trends of the R_a level observed are similar on each face. As this is a second order effect and systematic, faces will no longer be distinguished in what follows. R_a will then be taken as the mean of the two faces. Some possible explanations for this effect are provided in supplementary material.

Micrographs of Figure 6 illustrate cross-sections in the x-z (Figure 6.a) and x-y (Figure 6.b) planes of TW samples for three offsets and for both strategies. These micrographs also show that the excessive roughness with a BF strategy is mainly due to protuberant or "flowing-outward" contour melt pools highlighted by black arrows in Figure 6, as observed on UTW samples. This "flowing-outward" behavior of the melt pools of the contours is not observed with a CF strategy, where the contours are well located. Melt pools of the contours of the last processed layer (top layer) show a different shape depending on the strategies. With a CF strategy, the top melt pools are pointing vertically (black dashed arrows in Figure 6.a). On the contrary, with a BF strategy, top melt pools are pointing more and more horizontally when the offset decreases. This effect indicates that on a given layer, the already solidified bulk melt pools with a BF strategy disturb the contour tracks. It tends to push out the contour melt pools towards the unmelted powder.

Figure 5 shows that the value of R_a in the case of a BF strategy converges towards the value of R_a in the case of a CF strategy for large offsets. However, an excessive increase of the offset, corresponding to a decrease of the overlap between the bulk hatching and contours, leads to porosities appearing between the bulk and contours (white arrows on Figure 6), affecting the sample structural integrity.

In order to more statistically quantify this effect, some samples were characterized by X-ray tomography. For each sample, a mean local density was computed for all y-z plane measurements. Figure 7 presents the mean local density of TW samples following the x-direction for both building strategies and for several offsets. This figure also shows two reconstructed volumes of TW samples with a 120 µm-offset, showing porosities. A decrease in the local density near the surface is observed, starting at an offset of 90 µm for both strategies. This drop becomes extremely significant for an offset of 120 µm, decreasing the mean local density to 92 % in BF strategy and 97 % in CF strategy, respectively. The reconstructed volumes of the TW samples built with a 120 µm offset clearly show a large number of sub-surface pores. Interestingly, an asymmetry in the local density is observed for the BF strategy as it was observed for roughness (Figure 5). This effect could be attributed to a small thermal effect due to the asymmetric process itself. Indeed, heat brought by the first processed contour (Figure 1) slightly increases the temperature of the already solidified top layer so that

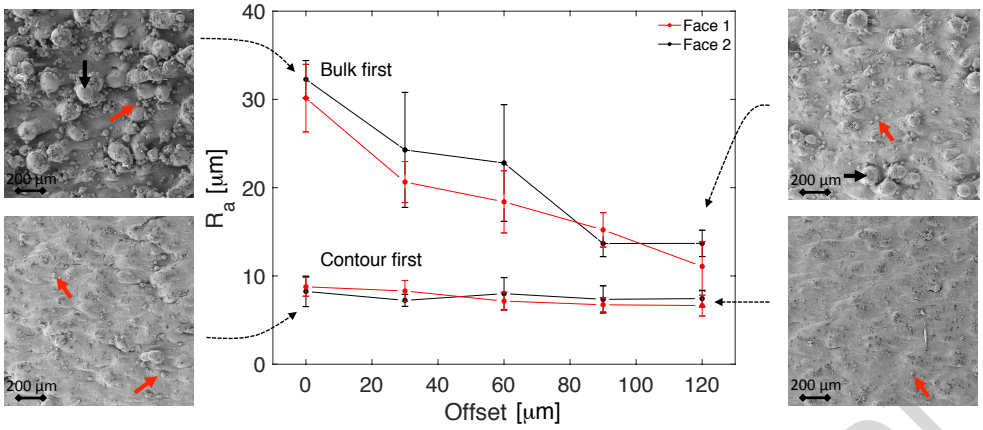

Figure 5. Evolution of the arithmetic roughness (R_a) of thin-walls (TW) samples as a function of the offset for both strategies. The TED value of the contours is the same than the TED value of the bulk hatching (232.5 W at 1200 mm/s, corresponding to 194 J/m). SEM micrographs show the surface of some TW samples (identified by black dashed arrows). Black arrows on the micrographs indicate examples of protuberant contour melt pools. Red arrows highlight examples of sintered powder particles.

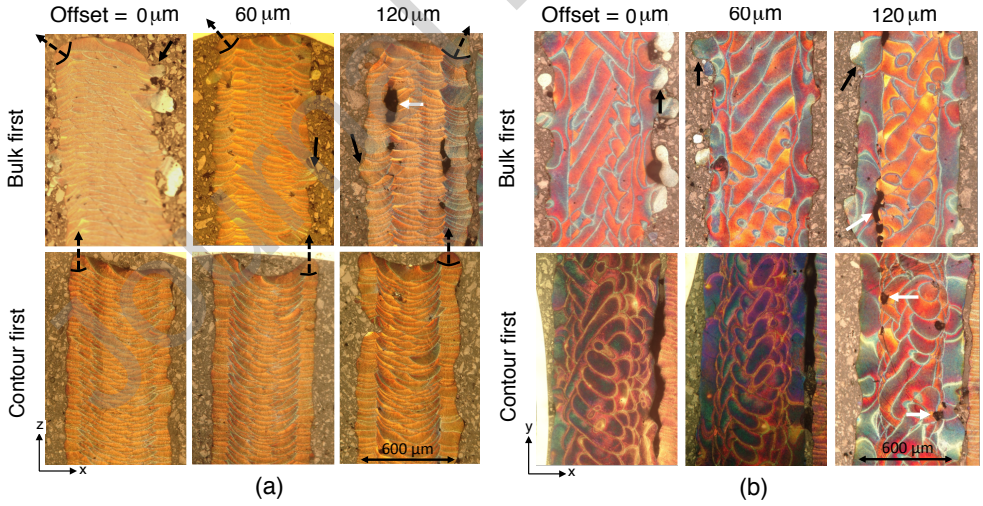

Figure 6. (a) Optical microscopy images of cross-sections in the x-z plane and (b) x-y plane corresponding to different building strategies. The dashed black arrows indicate the orientation of contour melt pools. The heat affected zone of the respective melt pools are highlighted in black. The full black arrows indicate examples of disturbed melt pools. The white arrows indicate porosities.

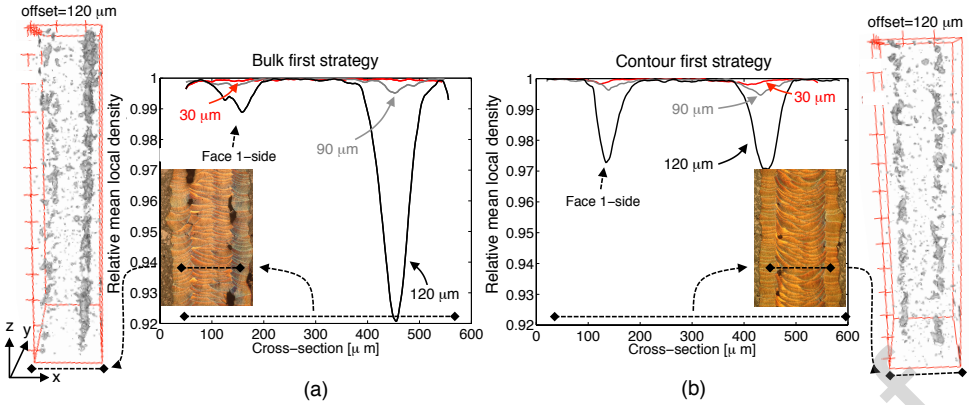

Figure 7. Local mean density of some TW samples following the x-direction, with (a) a BF strategy and (b) a CF strategy. Reconstructed volumes for an offset of 120 µm show a huge amount of porosities (depicted in grey). Optical microscopy images show a cross-section in the x-z plane of TW samples built with an offset of 120 µm.

the initial temperature (T_0) of the second contour is slightly higher than the initial temperature of the first processed contour, leading to a slightly larger melt pool. This effect is limited in the CF strategy as there is no solidified material between the contours, and thus less heat conduction towards the second processed contour.

The offset and the building strategies have a clear impact on the level of roughness. Figure 8 shows the impact of the TED level value chosen for the contours on R_a for three offsets and in the case of both strategies. In the case of a BF strategy (Figure 8.a), the level of TED and the offset have a first order effect on the level of roughness. R_a increases with TED for low TED values then decreases for high TED values, for the two smaller offsets (0 and 60 µm). R_a slightly increases then decreases with TED for the 120 µm-offset. The highest level of roughness is obtained with an offset of 0 µm.

For the CF strategy (Figure 8.b), only the level of TED has a first order effect. Indeed, R_a always decreases with TED. The effect of the offset on R_a is rather minor except at low TED level.

The highest level of roughness is observed with an offset of 0 µm, as it is the case with the BF strategy. This offset is a particular case since it means that there is no distance between contours and the bulk, i.e. the bulk (respectively contours) re-melts contours (respectively the bulk) in CF (respectively BF) strategy. The laser parameters selected for the bulk could then also have an influence on R_a and have been investigated.

3.4. ***Thin walls: effect of bulk parameters***

In order to study the effect of the bulk scanning parameters on the level of roughness, samples were processed with fixed contour parameters with a TED level of 194 J/m (232.6 W with a scan speed of 1200 mm/s) following both strategies and with variable bulk TED levels for three offset conditions. Figure 9 presents the evolution of

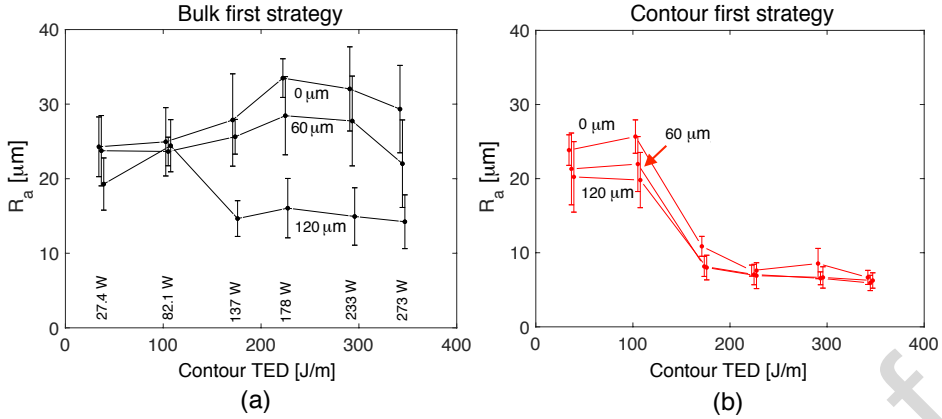

Figure 8. Evolution of R_a as a function of contour TED level and strategies, for three different offsets at fixed contour scan speed (800 mm/s). (a) Bulk first strategy, (b) contour first strategy.

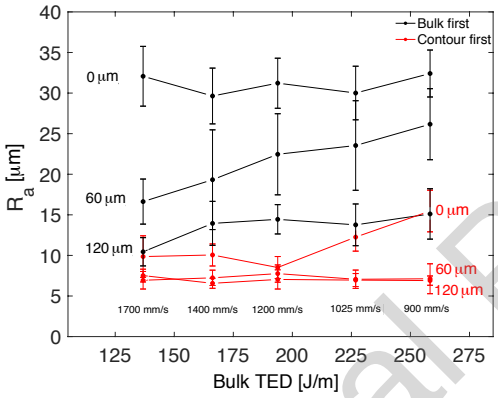

Figure 9. Effect of the bulk scanning parameters on R_a for three offsets as a function of bulk TED level for (in black) a bulk first strategy and for (in red) a contour first strategy. Bulk TED level is varied by changing the scanning speed only (indicated on the graph). Contour parameters are fixed at 85 % of P_{max} and 1200 mm/s.

R_a as a function of the bulk TED level for different offsets and strategies. The level of TED was increased by decreasing the scanning speed from 1700 mm/s to 800 mm/s.

With a BF strategy, when there is no offset between bulk tracks and contour tracks, R_a is large ($\sim$ 32 µm), whatever the bulk TED value (Figure 9.a). In the case of an offset, R_a slightly increases with the value of the bulk TED level. In the case of a CF strategy, the offset has a limited effect on R_a.

A small increase of R_a is observed for a 0 µm-offset when the bulk TED value becomes higher than the contour TED value (Figure 9). Similarly to the analysis of the influence of the contour parameters, the offset and bulk TED level are first order parameters for the BF strategy while only the bulk TED level has a significant effect with a CF strategy.

3.5. ***Trade-off between hardness and roughness***

The lowest level of roughness measured on TW samples was 5.9 µm (for a CF strategy, a 90 µm-offset and a TED value of 341 J/m). This level of R_a is higher than the lowest R_a level obtained with SWT samples. Even tough parameters leading to the lowest level of R_a for SWT samples are out of the process windows, a set of parameters corresponding to keyhole conditions (246 W at 300 mm/s, giving a TED level of 820 J/m) was tested on TW samples contours with both strategies and for a cube with CF strategy. Figure 10 presents the measured roughness and hardness of those samples. SWT sample corresponding to the same level of TED is also shown as a reference. Hardness was measured both on contours and on the bulk hatching. The TW-CF and cube-CF samples present the lowest R_a values measured in the present work, i.e. 4.2 µm and 3.9 µm, respectively (Figure 10.b). The TW-BF sample presents a R_a level of 8.6 µm. This is twice as rough as for the TW-CF sample, but it is still the best level of roughness in the case of the BF strategy.

As expected from the previous observations on SWT samples, there is a substantial hardness shift between the bulk and the contours for the TW samples (in the case of both strategies) and for the cube (Figure 10.b) due to different process parameters, leading to a change in the microstructure (See supplementary materials). Hardness measured on TW samples and cube bulk hatching are similar (136 HV). The lowest contour hardness is measured on the TW-CF sample (119 HV) but it is still higher than the hardness of the SWT sample (109 HV), while contour hardness of TW-BF sample and cube are very similar (∼126 HV). Figure 11 presents representative optical microscopy images of each sample. They clearly show that the process parameters lead to a keyhole mode, leaving a lot of large porosities in the middle of the melt pools. It also shows that the width of the TW samples is larger than the fixed width as the melt pools are very large in keyhole mode (Figure 10). This very high energy mode limits the porosities coming from a bad overlap between the bulk and the contours but brings new kind of porosities due to melt pool instability. The different level of hardness between contours and bulk resulting from the different microstructures might be a problem for the global mechanical behaviour, especially in thin elements and will need further investigation.

Surprisingly, conditions bringing keyholes are thus the solution to reach a low level of roughness. However, the resulting sub-surface porosities can be an issue for the mechanical performances of the samples. Figure 12 shows optical microscopy images of TW samples processed with an increasing level of TED. These micrographs show a drastic increase of the porosities due to the formation of keyholes when TED level increases. This leads to a trade-off between the level of roughness and the amount of sub-surface porosities. In this case, TW sample with contour TED of 684 J/m is a better option than TW sample with contour TED of 773 J/m, even though R_a is higher.

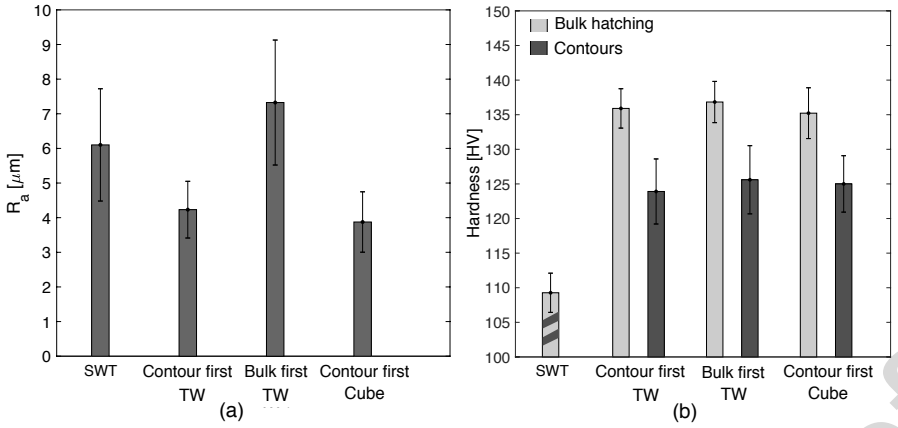

Figure 10. (a) Arithmetic roughness and (b) hardness measured on SWT and TW samples with CF and BF strategies and on a cube with CF strategy. Contour TED level is 820 J/m while bulk hatching TED level is 194 J/m. The offset was set to 90 µm for the TW sample and the cube.

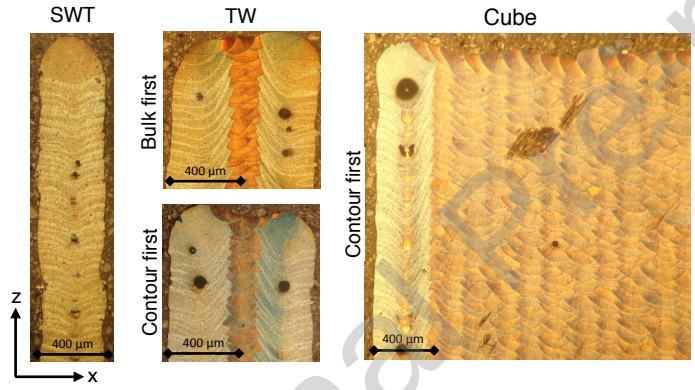

Figure 11. Optical microscopy images of SWT, TW and cube samples. Same samples as in Figure 10.

3.6. ***Assessment of the formation of the vertical roughness***

The vertical arithmetic roughness of L-PBF samples is a topographical measurement of the side of the contour melt pools. Any parameter impacting the morphology of the contour melt pools should then have an impact on the roughness. The analysis of SWT samples showed that the lowest level of R_a is attained in or near unstable melt pool track conditions, i.e. when TED level reaches the keyhole conditions (Figure 2). The reason is geometric and is related to the radius of curvature of the melt pools. This is illustrated in Figure 13, which presents schematically SWT morphologies for different conditions. In the process window (Figure 13.a), R_a decreases with TED (Figure 2) since the melt pool width increases and so does the radius of curvature. When the melt pool becomes unstable, as it is the case in balling conditions (Figure 13.b), the side profile becomes also unstable, increasing R_a. In keyhole conditions, i.e. at very high TED level, the radius of curvature of the melt pools is so large

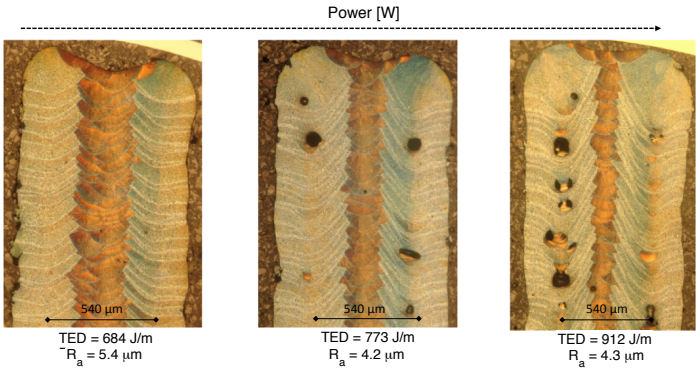

Figure 12. Optical microscopy images of TW samples with contours processed near or in keyhole conditions. Increasing the contour TED improves R_a but many sub-surface porosities appear.

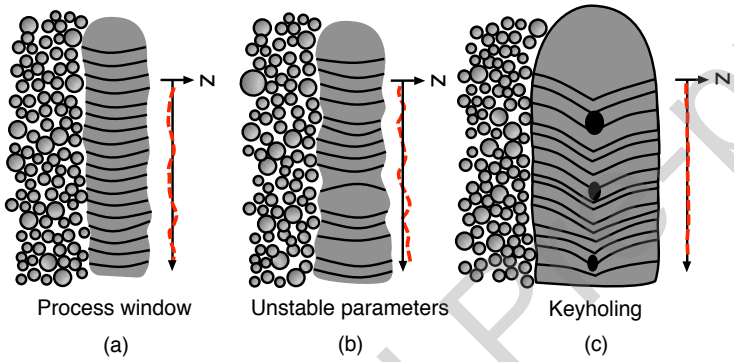

Figure 13. Schematic representation of cross-sections and profiles of SWT samples for (a) process parameters in the process window, (b) outside the process window (e.g. balling conditions) and (c) in keyhole conditions. The dashed red curves is a schematic representation of the expected roughness.

that the side profile appears flat, inducing a very low level of roughness. However, the instability within the melt pools causes the contour melt pool tracks to end up with huge porosities, which might reduce mechanical properties, particularly fatigue life (5). Moreover, the subsequent coarsening of the microstructure due to a longer time at high temperatures leads to a drastic hardness drop. Increasing the level of TED above the keyhole conditions cancels the benefit of large melt pools due to a progressive increase of sintered powder particles on the melt pool sides.

Another factor influencing the melt pool morphology has been highlighted with UTW samples. The distance between two melt pools was found to be a key factor inducing roughness. Figure 14 presents a schematic representation of the processing layer in the case of a UTW sample and two optical microscopy images of real samples showing the last processed layer. When the second contour is processed (Figure 14.c), its melt pool is disturbed by the first contour already solidified and seems to point outward. An asymmetric morphology between both tracks is in fact well observed

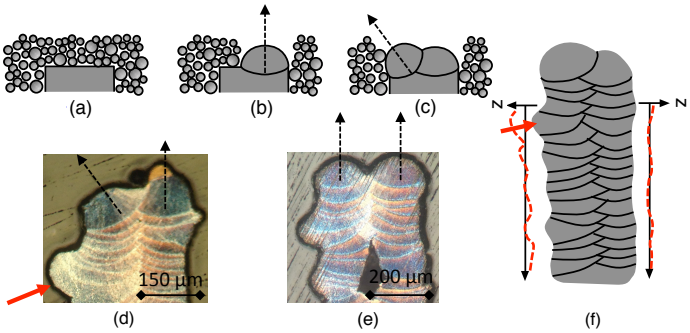

Figure 14. Schematic representation of the processing steps of a new layer of an UTW samples, consisting of (a) a deposition of a new layer of powder, (b) solidification of the first track and (c) solidification of the second track. (d, e) Optical microscopy images of the top layer of a UTW sample processed at 194 J/m for a distance between tracks of (d) 160 µm and (e) 190 µm. (f) Schematic representation of the cross-section of a UTW sample and its roughness profile on both sides. Red arrows indicate melt pools which increase dramatically the roughness.

on the samples (Figure 14.d). This observation has been experimentally confirmed in the case of an UTW sample processed with a laser track starting point shifted for each layer, following the UTW diagonal, as illustrated in Figure 15. A pattern due to a difference in roughness is clearly visible on each face. In some conditions, melt pools of the second contour extend outward (red arrows in Figure 14.f) too much which leads to an excessive roughness. When the distance between tracks increases, the asymmetry decreases but pores due to a bad overlapping appear (Figure 14.e).

In the case of TW samples, factors influencing the roughness are also depending on the same two factors. The level of TED tends to decrease the roughness by increasing the melt pool size while increasing the offset reduces interactions between contours and bulk hatching melt pools, thus decreasing the roughness. Moreover, increasing the melt pool size decreases the offset and should then counteract the beneficial geometrical effect of large melt pools. However, the importance of those effects depends on the adopted strategy.

Figure 16 schematically represents the difference between both strategies. In BF strategy, the melt pools of the contours are influenced by the solidified melt pools of the bulk hatching. Indeed, the solidified bulk tracks impact the wetting of the melt pools of the contours. In the case of a larger offset, the interactions between the contour and bulk melt pools are less significant. However, increasing the offset also increases the amount of sub-surface porosities due to a bad overlapping (30; 72) between the bulk tracks and the contour tracks, which is expected to be detrimental to the mechanical properties (particularly fatigue). Cracks can also easily initiate fracture in tensile tests and thus reduce the mechanical quality of the parts (40).

Micrographs of Figure 16.(a) illustrate cross-sections of CF-TW and BF-TW samples on which the bulk hatching and the contours of the last layer were not processed. In the case of the BF strategy, the solidified bulk tracks will disturb the melt pools of

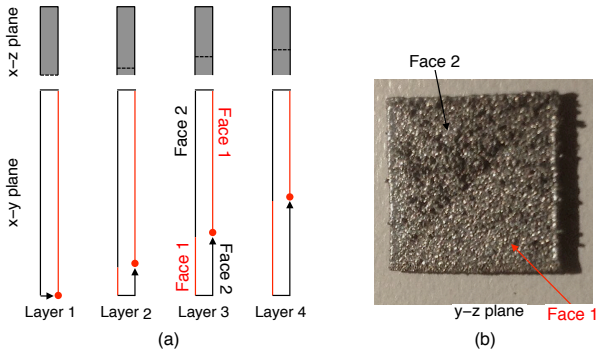

Figure 15. UTW sample processed with a starting point track shifted at each layer. (a) Schematic slicing of the UTW samples, showing the laser starting points (red dots) in the x-y plane and the corresponding layers in the x-z plane. The red tracks indicate the first track (corresponding to face 1) while the black ones indicate the second track (corresponding to face 2). (b) Picture of the UTW sample processed with a level of TED = 194 J/m.

the contours. A large offset limits the impact of those solidified tracks and thus the roughness. As for the UTW samples, this can be observed by the contour melt pools orientation (dashed arrows in Figure 16.a) of the last processed layer. In the case of the CF strategy, contour melt pools act as an 'overflow barrier'. The offset has no more effect as long as the bulk TED level is equal or lower than the contour TED level. Indeed, for a small offset, the bulk hatching can re-melt the contours (Figure 16.b). In this case, roughness increases since there are no more contours (Figure 9, CF with a 0 µm-offset).

Increasing the level of TED with a CF strategy decreases the level of roughness (Figure 8.b) due to a geometrical effect. The same trend is observed in the case of the BF strategy when the offset is large enough. For smaller offsets, the trends are different because the increase of the melt pool size with the level of TED decreases the offset and thus increases the roughness (Figure 8.a). For a large level of TED (above 220 J/m), the positive geometrical effect overpasses the negative effect of the decreasing offset, thus reducing the level of roughness.

Small variations of the solidified bulk melt pools in the case of a BF strategy, due to slight variations of some parameters (powder size and compaction, layers rotation, laser fluctuation...) (46; 73) can induce an uneven side profile of the bulk hatching (Figure 16.b). It impacts slightly the roughness since this uneven side profile disturbs the wetting behavior of the contour melt pools. It is worth noting that powder denudation (27; 71) in BF strategy (Figure 1.b) can also have a small impact on the contour melt pool geometry due to the induced slight lack of powder near the contour.

4. Conclusions

The present study addressed the origin of the vertical roughness in L-PBF AlSi10Mg alloy components. Three different structures have been considered to address the key

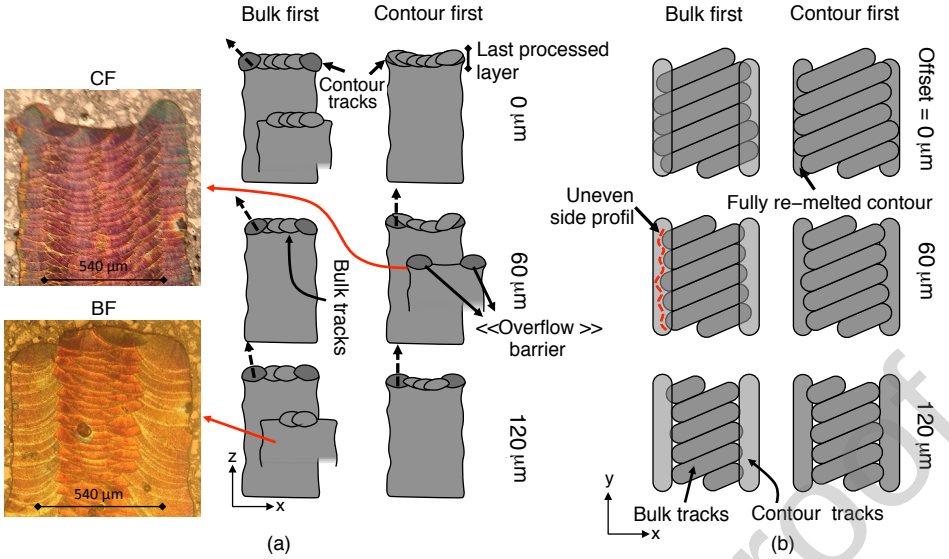

Figure 16. Schematic representation of the contour laser track and bulk laser track as a function of the strategies and of the offset in the (a) x-z plane and in the (b) x-y plane.

factors impacting the level of roughness.

Single wall tracks (SWT) specimens have been used to assess the effect of the track energy density (TED) on the roughness and on the hardness. It has been shown that increasing the level of TED has a beneficial impact on the reduction of the roughness due to a geometrical effect. A large melt pool leads to a more vertical side-profile than a small melt-pool. However, it has a detrimental effect on the hardness due to the coarsening of the microstructure. The optimum level of TED for low roughness was found to be at the onset of the keyhole conditions. Increasing the TED level above that value increases the amount of sintered powder particles on the side of SWT samples and thus cancels the benefit of the geometrical effect. Moreover, it brings a lot of porosities induced by keyhole laser conditions.

Ultra thin wall (UTW) specimens have been used to study the effect of parallel tracks on the roughness. Distance or offset between melt pools was found to be a key element to reduce the roughness. A larger offset between melt pools is always beneficial to reduce the level of roughness. Indeed, the wetting occurring between a melt pool and a solidified melt pool next to it leads to a slight overflow of the liquid, increasing the roughness.

Thin wall (TW) samples with contours and bulk hatching have been used to analyze the impact of the TED level and of the offset together. The two possible strategies, contour first (CF) or bulk first (BF) have been investigated. With a CF strategy, only the level of TED has a first order impact. Increasing the TED level lowers the level of roughness. With a BF strategy, both the offset and the TED level have a first order effect. Increasing the offset allows reducing the wetting issue between the contour melt pool and the solidified bulk hatching melt pools but increases

porosities due to a bad overlapping between the contours and the bulk hatching. However, increasing the TED level has a mixed effect. On the one hand, it tends to reduce the roughness due to a geometrical effect. On the other hand, increasing the size of the melt pools also decreases the offset and thus affects negatively the roughness. In the different conditions investigated for TW specimens, a CF strategy always gave the lowest vertical roughness compared to a BF strategy. This strategy should then be preferably used to process any object. A relatively high level of TED has also to be used for the contours to obtain a smooth surface. The difference in hardness between contours and bulk induced by the different parameters might be a problem for the mechanical properties, especially in thin elements, as damaging mechanisms depend on the microstructure (74; 75), and requires further investigations.

Acknowledgments

The present work is supported by the Walloon Region through the Skywin project 'InHex'. The authors also acknowledge the financial support from the European Funds for Regional Developments (FEDER) and the Walloon Region in the framework of the operational program Wallonie-2020.EU (project : IAWATHA/AManUMater, n101628-722943). This work has been performed with the help of the Lacami technological platform of UCLouvain. The authors also thank the Wallonia Electronics and Communications Measurements platform (WELCOME) of UCLouvain for the use of the white light interferometer.

References

[1] Tarasankar DebRoy, HL Wei, JS Zuback, T Mukherjee, JW Elmer, JO Milewski, Allison Michelle Beese, A Wilson-Heid, A De, and W Zhang. Additive manufacturing of metallic components–process, structure and properties. *Progress in Materials Science*, 92:112–224, 2018.

[2] Nesma T Aboulkhair, Ian Maskery, Chris Tuck, Ian Ashcroft, and Nicola M Everitt. Improving the fatigue behaviour of a selectively laser melted aluminium alloy: Influence of heat treatment and surface quality. *Materials & Design*, 104:174–182, 2016.

[3] Ana D Brandão, Johannes Gumpinger, Michael Gschweitl, Christoph Seyfert, Peter Hofbauer, and Tommaso Ghidini. Fatigue properties of additively manufactured alsi10mg–surface treatment effect. *Procedia Structural Integrity*, 7:58–66, 2017.

[4] Sara Bagherifard, Niccolò Beretta, Stefano Monti, Martina Riccio, Michele Bandini, and Mario Guagliano. On the fatigue strength enhancement of additive manufactured alsi10mg parts by mechanical and thermal post-processing. *Materials & Design*, 145:28–41, 2018.

[5] Emilie Beevers, Ana D Brandão, Johannes Gumpinger, Michael Gschweitl, Christoph Seyfert, Peter Hofbauer, Thomas Rohr, and Tommaso Ghidini. Fatigue properties and material characteristics of additively manufactured alsi10mg–effect of the contour parameter on the microstructure, density, residual stress, roughness and mechanical properties. *International Journal of Fatigue*, 117:148–162, 2018.

[6] Marina Cabrini, Sergio Lorenzi, Tommaso Pastore, Simone Pellegrini, Matteo Pavese, Paolo Fino, Elisa Paola Ambrosio, Flaviana Calignano, and Diego

Manfredi. Corrosion resistance of direct metal laser sintering alsimg alloy. *Surface and Interface Analysis*, 48(8):818–826, 2016.

[7] Avi Leon and Eli Aghion. Effect of surface roughness on corrosion fatigue performance of alsi10mg alloy produced by selective laser melting (slm). *Materials Characterization*, 131:188–194, 2017.

[8] P Fathi, M Rafieazad, X Duan, M Mohammadi, and AM Nasiri. On microstructure and corrosion behaviour of alsi10mg alloy with low surface roughness fabricated by direct metal laser sintering. *Corrosion Science*, 2019.

[9] Flaviana Calignano, D Manfredi, EP Ambrosio, Luca Iuliano, and Paolo Fino. Influence of process parameters on surface roughness of aluminum parts produced by dmls. *The International Journal of Advanced Manufacturing Technology*, 67(9-12):2743–2751, 2013.

[10] Lin-zhi Wang, Sen Wang, and Jiao-jiao Wu. Experimental investigation on densification behavior and surface roughness of alsi10mg powders produced by selective laser melting. *Optics & Laser Technology*, 96:88–96, 2017.

[11] Ahmed H Maamoun, Mohamed Elbestawi, Goulnara K Dosbaeva, and Stephen C Veldhuis. Thermal post-processing of alsi10mg parts produced by selective laser melting using recycled powder. *Additive Manufacturing*, 21:234–247, 2018.

[12] Ahmed Maamoun, Yi Xue, Mohamed Elbestawi, and Stephen Veldhuis. Effect of selective laser melting process parameters on the quality of al alloy parts: Powder characterization, density, surface roughness, and dimensional accuracy. *Materials*, 11(12):2343, 2018.

[13] Mohsen Mohammadi and Hamed Asgari. Achieving low surface roughness alsi10mg_200c parts using direct metal laser sintering. *Additive Manufacturing*, 20:23–32, 2018.

[14] Wenhui Yu, Swee Leong Sing, Chee Kai Chua, and Xuelei Tian. Influence of re-melting on surface roughness and porosity of alsi10mg parts fabricated by selective laser melting. *Journal of Alloys and Compounds*, 792:574–581, 2019.

[15] Arfan Majeed, Jingxiang Lv, Yingfeng Zhang, Muhammad Muzamil, Ali Waqas, Khalid Shamim, Muhammad Ejaz Qureshi, and Fahad Zafar. An investigation into the influence of processing parameters on the surface quality of alsi10mg parts by slm process. In *2019 16th international bhurban conference on applied sciences and technology (IBCAST)*, pages 143–147. IEEE, 2019.

[16] Arfan Majeed, Altaf Ahmed, Abdus Salam, and Muhammad Zakir Sheikh. Surface quality improvement by parameters analysis, optimization and heat treatment of alsi10mg parts manufactured by slm additive manufacturing. *International Journal of Lightweight Materials and Manufacture*, 2(4):288–295, 2019.

[17] Bao-Qiang Li, Zhonghua Li, Peikang Bai, Bin Liu, and Zezhou Kuai. Research on surface roughness of alsi10mg parts fabricated by laser powder bed fusion. *Metals*, 8(7):524, 2018.

[18] Tao Yang, Tingting Liu, Wenhe Liao, Eric MacDonald, Huiliang Wei, Xiangyuan Chen, and Liyi Jiang. The influence of process parameters on vertical surface roughness of the alsi10mg parts fabricated by selective laser melting. *Journal of Materials Processing Technology*, 266:26–36, 2019.

[19] PB Bacchewar, SK Singhal, and PM Pandey. Statistical modelling and optimization of surface roughness in the selective laser sintering process. *Proceedings of the Institution of Mechanical Engineers, Part B: Journal of Engineering Manufacture*, 221(1):35–52, 2007.

[20] Alberto Boschetto, Luana Bottini, and Francesco Veniali. Roughness modeling of alsi10mg parts fabricated by selective laser melting. *Journal of Materials Processing Technology*, 241:154–163, 2017.

[21] Xuesong Han, Haihong Zhu, Xiaojia Nie, Guoqing Wang, and Xiaoyan Zeng. Investigation on selective laser melting alsi10mg cellular lattice strut: molten pool morphology, surface roughness and dimensional accuracy. *Materials*, 11(3):392, 2018.

[22] A Barari, HA Kishawy, F Kaji, and MA Elbestawi. On the surface quality of additive manufactured parts. *The International Journal of Advanced Manufacturing Technology*, 89(5-8):1969–1974, 2017.

[23] F Calignano. Investigation of the accuracy and roughness in the laser powder bed fusion process. *Virtual and Physical Prototyping*, 13(2):97–104, 2018.

[24] Charlotte de Formanoir, Umberto Paggi, Thomas Colebrants, Lore Thijs, Guichuan Li, Kim Vanmeensel, and Brecht Van Hooreweder. Increasing the productivity of laser powder bed fusion: influence of the hull-bulk strategy on part quality, microstructure and mechanical performance of ti-6al-4v. *Additive Manufacturing*, page 101129, 2020.

[25] I Yadroitsev, Pavel Krakhmalev, I Yadroitsava, Sten Johansson, and I Smurov. Energy input effect on morphology and microstructure of selective laser melting single track from metallic powder. *Journal of Materials Processing Technology*, 213(4):606–613, 2013.

[26] Karolien Kempen, Lore Thijs, Jan Van Humbeeck, and J-P Kruth. Processing alsi10mg by selective laser melting: parameter optimisation and material characterisation. *Materials Science and Technology*, 31(8):917–923, 2015.

[27] Nesma T Aboulkhair, Ian Maskery, Chris Tuck, Ian Ashcroft, and Nicola M Everitt. On the formation of alsi10mg single tracks and layers in selective laser melting: Microstructure and nano-mechanical properties. *Journal of Materials Processing Technology*, 230:88–98, 2016.

[28] Eleftherios Louvis, Peter Fox, and Christopher J Sutcliffe. Selective laser melting of aluminium components. *Journal of Materials Processing Technology*, 211(2):275–284, 2011.

[29] Lore Thijs, Karolien Kempen, Jean-Pierre Kruth, and Jan Van Humbeeck. Fine-structured aluminium products with controllable texture by selective laser melting of pre-alloyed alsi10mg powder. *Acta Materialia*, 61(5):1809–1819, 2013.

[30] Nesma T Aboulkhair, Nicola M Everitt, Ian Ashcroft, and Chris Tuck. Reducing porosity in alsi10mg parts processed by selective laser melting. *Additive Manufacturing*, 1:77–86, 2014.

[31] Pei Wei, Zhengying Wei, Zhen Chen, Jun Du, Yuyang He, Junfeng Li, and Yatong Zhou. The alsi10mg samples produced by selective laser melting: single track, densification, microstructure and mechanical behavior. *Applied surface science*, 408:38–50, 2017.

[32] F Calignano, G Cattano, and D Manfredi. Manufacturing of thin wall structures in alsi10mg alloy by laser powder bed fusion through process parameters. *Journal of Materials Processing Technology*, 255:773–783, 2018.

[33] Pierre Lhuissier, Xavier Bataillon, Camille Maestre, Julien Sijobert, Elodie Cabrol, Philippe Bertrand, Elodie Boller, Alexander Rack, Jean-Jacques Blandin, Luc Salvo, et al. In situ 3d x-ray microtomography of laser-based powder-bed fusion (l-pbf)-a feasibility study. *Additive Manufacturing*, page 101271, 2020.

[34] Luhao Yuan, Dongdong Gu, Kaijie Lin, Qing Ge, Xinyu Shi, Haoran Wang, and Kaiming Hu. Influence of structural features on processability, microstructures, chemical compositions, and hardness of selective laser melted complex thin-walled components. *The International Journal of Advanced Manufacturing Technology*, 109(5):1643–1654, 2020.

[35] Idan Rosenthal, Adin Stern, and Nachum Frage. Microstructure and mechanical properties of alsi10mg parts produced by the laser beam additive manufacturing (am) technology. *Metallography, Microstructure, and Analysis*, 3(6):448–453, 2014.

[36] Michaela Fousová, Drahomír Dvorskỳ, Alena Michalcová, and Dalibor Vojtěch. Changes in the microstructure and mechanical properties of additively manufactured alsi10mg alloy after exposure to elevated temperatures. *Materials Characterization*, 137:119–126, 2018.

[37] Ming Tang and Petrus Christiaan Pistorius. Anisotropic mechanical behavior of alsi10mg parts produced by selective laser melting. *Jom*, 69(3):516–522, 2017.

[38] YJ Liu, Z Liu, Y Jiang, GW Wang, Yang Yang, and LC Zhang. Gradient in microstructure and mechanical property of selective laser melted alsi10mg. *Journal of Alloys and Compounds*, 735:1414–1421, 2018.

[39] Le Zhou, Abhishek Mehta, Esin Schulz, Brandon McWilliams, Kyu Cho, and Yongho Sohn. Microstructure, precipitates and hardness of selectively laser melted alsi10mg alloy before and after heat treatment. *Materials Characterization*, 143:5–17, 2018.

[40] Karolien Kempen, Lore Thijs, Jan Van Humbeeck, and Jean-Pierre Kruth. Mechanical properties of alsi10mg produced by selective laser melting. *Physics Procedia*, 39:439–446, 2012.

[41] Nesma T Aboulkhair, Ian Maskery, Chris Tuck, Ian Ashcroft, and Nicola M Everitt. The microstructure and mechanical properties of selectively laser melted alsi10mg: The effect of a conventional t6-like heat treatment. *Materials Science and Engineering: A*, 667:139–146, 2016.

[42] A Iturrioz, E Gil, MM Petite, F Garciandia, AM Mancisidor, and M San Sebastian. Selective laser melting of alsi10mg alloy: influence of heat treatment condition on mechanical properties and microstructure. *Welding in the World*, 62(4):885–892, 2018.

[43] Wei Li, Shuai Li, Jie Liu, Ang Zhang, Yan Zhou, Qingsong Wei, Chunze Yan, and Yusheng Shi. Effect of heat treatment on alsi10mg alloy fabricated by selective laser melting: Microstructure evolution, mechanical properties and fracture mechanism. *Materials Science and Engineering: A*, 663:116–125, 2016.

[44] I Yadroitsev, A Gusarov, I Yadroitsava, and I Smurov. Single track formation in selective laser melting of metal powders. *Journal of Materials Processing Technology*, 210(12):1624–1631, 2010.

[45] Suman Das. Physical aspects of process control in selective laser sintering of metals. *Advanced Engineering Materials*, 5(10):701–711, 2003.

[46] Carolin Körner, Elham Attar, and Peter Heinl. Mesoscopic simulation of selective beam melting processes. *Journal of Materials Processing Technology*, 211(6):978–987, 2011.

[47] Guanqun Yu, Dongdong Gu, Donghua Dai, Mujian Xia, Chenglong Ma, and Qimin Shi. On the role of processing parameters in thermal behavior, surface morphology and accuracy during laser 3d printing of aluminum alloy. *Journal of Physics D: Applied Physics*, 49(13):135501, 2016.

[48] Saad A Khairallah and Andy Anderson. Mesoscopic simulation model of selective laser melting of stainless steel powder. *Journal of Materials Processing Technology*, 214(11):2627–2636, 2014.

[49] Saad A Khairallah, Andrew T Anderson, Alexander Rubenchik, and Wayne E King. Laser powder-bed fusion additive manufacturing: Physics of complex melt flow and formation mechanisms of pores, spatter, and denudation zones. *Acta Materialia*, 108:36–45, 2016.

[50] Min Zheng, Lei Wei, Jing Chen, Qiang Zhang, Chongliang Zhong, Xin Lin, and Weidong Huang. A novel method for the molten pool and porosity formation modelling in selective laser melting. *International Journal of Heat and Mass Transfer*, 140:1091–1105, 2019.

[51] Noriko Read, Wei Wang, Khamis Essa, and Moataz M Attallah. Selective laser melting of alsi10mg alloy: Process optimisation and mechanical properties development. *Materials & Design (1980-2015)*, 65:417–424, 2015.

[52] U Tradowsky, J White, RM Ward, N Read, W Reimers, and MM Attallah. Selective laser melting of alsi10mg: Influence of post-processing on the microstructural and tensile properties development. *Materials & Design*, 105:212–222, 2016.

[53] Jean-Pierre Kruth, Ludo Froyen, Jonas Van Vaerenbergh, Peter Mercelis, Marleen Rombouts, and Bert Lauwers. Selective laser melting of iron-based powder. *Journal of materials processing technology*, 149(1-3):616–622, 2004.

[54] Leonhard Hitzler, Christoph Janousch, Jochen Schanz, Markus Merkel, Burkhard Heine, Florian Mack, Wayne Hall, and Andreas Öchsner. Direction and location dependency of selective laser melted alsi10mg specimens. *Journal of Materials Processing Technology*, 243:48–61, 2017.

[55] Peter de Groot. Coherence scanning interferometry. In *Optical measurement of surface topography*, pages 187–208. Springer, 2011.

[56] Jon Petzing, Jeremy Coupland, and Richard K Leach. *Good practice guide No. 116, The measurement of rough surface topography using coherence scanning interferometry*. National Physical Laboratory, 2010.

[57] Andrew Townsend, N Senin, Liam Blunt, RK Leach, and JS Taylor. Surface texture metrology for metal additive manufacturing: a review. *Precision Engineering*, 46:34–47, 2016.

[58] Nicola Senin, Adam Thompson, and Richard K Leach. Characterisation of the topography of metal additive surface features with different measurement technologies. *Measurement Science and Technology*, 28(9):095003, 2017.

[59] Adam Thompson, Nicola Senin, Claudiu Giusca, and Richard Leach. Topography of selectively laser melted surfaces: a comparison of different measurement methods. *CIRP Annals*, 66(1):543–546, 2017.

[60] Carlos Gomez, Rong Su, Adam Thompson, Jack DiSciacca, Simon Lawes, and Richard K Leach. Optimization of surface measurement for metal additive manufacturing using coherence scanning interferometry. *Optical Engineering*, 56(11):111714, 2017.

[61] J-Y Buffiere, E Maire, J Adrien, J-P Masse, and E Boller. In situ experiments with x ray tomography: an attractive tool for experimental mechanics. *Experimental mechanics*, 50(3):289–305, 2010.

[62] Jérôme Adrien, Sylvain Meille, Solène Tadier, Eric Maire, and Layla Sasaki. In-situ x-ray tomographic monitoring of gypsum plaster setting. *Cement and Concrete Research*, 82:107–116, 2016.

[63] Johannes Schindelin, Ignacio Arganda-Carreras, Erwin Frise, Verena Kaynig, Mark Longair, Tobias Pietzsch, Stephan Preibisch, Curtis Rueden, Stephan Saalfeld, Benjamin Schmid, et al. Fiji: an open-source platform for biological-image analysis. *Nature methods*, 9(7):676, 2012.

[64] Wayne E King, Holly D Barth, Victor M Castillo, Gilbert F Gallegos, John W Gibbs, Douglas E Hahn, Chandrika Kamath, and Alexander M Rubenchik. Observation of keyhole-mode laser melting in laser powder-bed fusion additive manufacturing. *Journal of Materials Processing Technology*, 214(12):2915–2925, 2014.

[65] Donghua Dai and Dongdong Gu. Effect of metal vaporization behavior on keyhole-mode surface morphology of selective laser melted composites using different protective atmospheres. *Applied Surface Science*, 355:310–319, 2015.

[66] Jieren Guan, Yehua Jiang, Xiaowei Zhang, and Xiaoyu Chong. Microstructural evolution and ebsd analysis of alsi10mg alloy fabricated by selective laser remelting. *Materials Characterization*, 161:110079, 2020.

[67] B Chen, SK Moon, X Yao, G Bi, J Shen, J Umeda, and K Kondoh. Strength and strain hardening of a selective laser melted alsi10mg alloy. *Scripta Materialia*, 141:45–49, 2017.

[68] Pauline Delroisse, Pascal J. Jacques, Eric Maire, Olivier Rigo, and Aude Simar. Effect of strut orientation on the microstructure heterogeneities in alsi10mg lattices processed by selective laser melting. *Scripta Materialia*, 141:32–35, 2017.

[69] I Rosenthal, R Shneck, and A Stern. Heat treatment effect on the mechanical properties and fracture mechanism in alsi10mg fabricated by additive manufacturing selective laser melting process. *Materials Science and Engineering: A*, 729:310–322, 2018.

[70] E Sert, L Hitzler, B Heine, M Merkel, E Werner, and A Öchsner. Influence of the heat treatment on the microstructure and hardness of additively manufactured alsi10mg samples. *Practical Metallography*, 56(2):91–105, 2019.

[71] I Yadroitsev and I Smurov. Surface morphology in selective laser melting of metal powders. *Physics Procedia*, 12:264–270, 2011.

[72] Ming Tang, P Chris Pistorius, and Jack L Beuth. Prediction of lack-of-fusion porosity for powder bed fusion. *Additive Manufacturing*, 14:39–48, 2017.

[73] Carolin Körner, Andreas Bauereiß, and Elham Attar. Fundamental consolidation mechanisms during selective beam melting of powders. *Modelling and Simulation in Materials Science and Engineering*, 21(8):085011, 2013.

[74] Lv Zhao, Juan Guillermo Santos Macías, Lipeng Ding, Hosni Idrissi, and Aude Simar. Damage mechanisms in selective laser melted alsi10mg under as built and different post-treatment conditions. *Materials Science and Engineering: A*, 764:138210, 2019.

[75] Juan Guillermo Santos Macías, Chola Elangeswaran, Lv Zhao, Brecht Van Hooreweder, Jérôme Adrien, Eric Maire, Jean-Yves Buffière, Wolfgang Ludwig, Pascal J Jacques, and Aude Simar. Ductilisation and fatigue life enhancement of selective laser melted alsi10mg by friction stir processing. *Scripta Materialia*, 170:124–128, 2019.

Authors statement

We are not interested in recognizing author individual contributions.

Declaration of interests

☒ The authors declare that they have no known competing financial interests or personal relationships that could have appeared to influence the work reported in this paper.

☐The authors declare the following financial interests/personal relationships which may be considered as potential competing interests: